International Journal of Solids and Structures 138 (2018) 87–96

Contents lists available at ScienceDirect

International Journal of Solids and Structures

journal homepage: www.elsevier.com/locate/ijsolstr

Experimental and modelling study of fatigue crack initiation in an aluminium beam with a hole under 4-point bending

Wenye Ye[a,b,*], Panos Efthymiadis[b,c], Christophe Pinna[c], Anxin Ma[a], Barbara Shollock[b], Richard Dashwood[d]

[a] Interdisciplinary Centre for Advanced Materials Simulation, Ruhr-University Bochum, Universitätsstr. 90 a, 44789 Bochum, Germany
[b] Warwick Manufacturing Group, International Manufacturing Centre, University of Warwick, Coventry CV4 7AL, UK
[c] Department of Mechanical Engineering, The University of Sheffield, Mappin Street, Sheffield S1 3JD, UK
[d] Vice Chancellor's Office, Coventry University, Coventry CV1 5FB, UK

ARTICLE INFO

Article history:
Received 16 May 2017
Revised 30 October 2017
Available online 10 January 2018

Keywords:
A. crack initiation
A. slip band
B. crystal plasticity
4-points bending test
Fatigue indicating parameter

ABSTRACT

Slip band formation and crack initiation during cyclic fatigue were investigated by in-situ experiments and non-local CPFEM simulations systematically. Experimental techniques including EBSD, digital image correlation (DIC) and SEM have been used to obtain consistent grain orientations, local strains, as well as the locations where slip bands and micro-cracks form on the sample surface. The realistic microstructure based on the EBSD map has been generated and used for finite element modelling. An advanced non-local crystal plasticity model, which considers the isotropic and kinematic hardening of the plastic strain gradient, has been adopted. The simulation results match well the corresponding experimental results. It was found that total strain and averaged slip on all slip systems, combined with accumulated slip on specific slip planes help predict the location and orientation of slip bands and micro-crack initiation correctly. Furthermore, a fatigue indicating parameter based on competition between maximum slip and the total slip has been proposed to reproduce the experimental observations.

1. Introduction

The fatigue life of metallic materials usually goes through three main stages as crack initiation, crack propagation and failure. The local microstructural features of the material determine the location sites for the appearance of cracks, which usually take place in these regions such as triple points, particle-matrix interfaces, pores and so called *weak* grains. Although crack initiation plays a dominant role in the whole process of fatigue, it has received relatively less attention than crack propagation. Nevertheless, many studies have been lately done in this field (e.g. Christ et al., 2009 and Sangid et al., 2011). Various experiments have been conducted to observe how cracks formed in the material, and a large number of numerical models have been established to predict crack initiation in past decades.

A large number of experiments with different materials under different loading conditions have been conducted through the years to observe micro-crack formation. For example, Bozek et al. (2008) studied the fatigue process on double edge-notched (DEN) specimens. They observed cracks in most of Al_7Cu_2Fe particles just after the first fatigue cycle. The observations are consistent with that of many others similar experiments reported in literature. Cheong et al. (2007) carried out a four-point bending fatigue test of an aluminum sample, which was subjected to high cycle fatigue (HCF) and the initial microstructure was characterized by EBSD analysis. Valuable investigation on crack initiation under uniform tensile stress have been carried out. Alexandre et al. (2004) and Findley (2005) showed that the crack initiation life depends on the relative sizes of the grains and inclusions. Alexandre et al. (2004) found that cracks formed only at slip bands for materials with large grain size. Jablonski (1981) found that crack initiation originated along persistent slip bands for a ceramic material; with these regions having more tendency to incubate cracks that those regions where the inclusion diameter was less than or equal to the grain size.

Many models have been proposed in the literature to predict crack incubation and growth. Tanaka and Mura (1981) assumed that crack initiation originates from slip bands, without considering the effect of cyclic hardening. Bozek et al. (2008) made

* Corresponding author at: Interdisciplinary Centre for Advanced Materials Simulation, Ruhr-University Bochum, Universitätsstr. 90 a, 44789 Bochum, Germany.
E-mail addresses: wenye.ye@ruhr-uni-bochum.de (W. Ye), P.Efthymiadis@warwick.ac.uk (P. Efthymiadis).

https://doi.org/10.1016/j.ijsolstr.2018.01.001

a probabilistic simulation of constituent particle cracking in a specimen. They used a reduced number of particles to simulate crack initiation and microstructurally small crack growth. Hochhalter et al. (2010) adopted two slip-based metrics to study crack initiation, one based on the slip on the dominant slip systems and the other on the summation of slip on all slip systems. They found that the metrics and local stresses are crucial to predict crack initiation. Many studies (Fine and Bhat, 2007; Mura and Nakasone, 1990; Tanaka and Mura, 1981; Bobylev et al., 2010; Xie et al., 2016) proposed that an energy barrier must be overcome during fatigue crack initiation to form the new crack surfaces.

Combining representative volume element (RVE) andcrystal plasticity finite element method (CPFEM) is a powerful tool which could be used to evaluate crack initiation and propagation inside a computational micro-mechanics framework (Anahid and Ghosh, 2013; Bache et al., 2010; Brahme et al., 2011; Dunne et al., 2007; Kuhlmann-Wilsdorf, 1999; Li et al., 2012; Repetto and Ortiz, 1997; Robert et al., 2012; Bennett and McDowell, 2003; Sweeney et al., 2013; Hoshide and Kusuura, 1998; Olfe et al., 2000). Li et al. (2015) utilised CPFEM in a RVE under cyclic loading to identify the weakest regions where cracks initiate and obtained a relationship between microstructure properties and an energy efficiency factor. Cheong et al. (2007) studied cracks inside a 4-point bending fatigue test specimen. Their model correctly predicted the crack initiation sites observed in the experiment. Based on the Tanaka–Mura model, Shenoy et al. (2007) investigated the fatigue life of a polycrystalline Ni-base superalloy by introducing the so-called fatigue indicating-parameters (FIPs). Using a Voronoi tessellation with 100 grains (Brückner-Foit and Huang, 2006) and the Tanaka–Mura model, Brückner-Foit and Huang (2006) studied the heterogeneous stress distribution and estimated the number of cycles to initiate fatigue cracks. Their approach was able to describe the whole process of crack fatigue life and revealed a relationship between crack initiation and the number of load cycles. Huang et al. (2007) extended the often used 2D model to a mesoscopic model close to 3D and found that, although the analysis became more complicated, the results for the crack density were quite similar to that from the 2D model. Full 3D models have also been developed in recent studies and showed the importance of using a 3D model in predicting the fatigue life. Navarro et al. (2014) compared the results of fatigue life estimation between 2D and 3D models. They concluded that the 3D model gave better results under certain conditions, but the 2D model also produced results similar to the experimental results. Manonukul and Dunne (2004) investigated the crack initiation in Ni-based alloy under high- and low-cycle fatigue considering grain morphology and crystallographic orientation. It was found that the formation of persistent slip bands (PSBs) and the accumulated plastic deformation are important mechanisms that drive fatigue crack initiation. Results also showed that crack initiation occurs at *weak* grains under both LCF and HCF. Cyclic plasticity is also important in predicting crack initiation. Several studies showed that the application of cyclic plasticity led sometimes to better predictions (Dunne et al., 2007; Manonukul et al., 2005; Tsutsumi et al., 2010; Kartal et al., 2014), than those obtained using accumulated plasticity for some materials. Till now there still exist challenges including: construction of proper microstructures of multiphase engineering materials for finite element modelling, development of crystal plasticity models considering hardening of strain gradients, and finding the relation between damage and micro-crack initiation with local stress and strain. The RVE generation methods in some studies (Becker and Panchanadeeswaran, 1995; Cheong et al., 2007; Weiland and Becker, 1999; Becker and Weiland, 2000; Bhattacharyya et al., 2001; Cheong and Busso, 2004; St-Pierre et al., 2008; Choi et al., 2013; Zhang et al., 2016) often include mapping EBSD data to a coarser regular finite mesh (Cheong et al., 2007) or generate a statistic type Voronoi tessellation considering grain size distribution (Kozaczek et al., 1995). Regular meshed RVEs of polycrystals contain steps and corners along grain boundaries which are physically unrealistic and inaccurate since the mechanical properties of grain boundaries are very much dependent on both local misorientations and the grain boundary plane's normal vector direction. Simulation results from this kind of RVEs have therefore limitations to predict deformation, strain localization and fatigue crack formation; as observed via in-situ testing.

In this paper, slip band formation and crack initiation were investigated by in-situ experiments and CPFEM simulations systematically. A Deben vertical bending equipment was used to conduct a 4-points bending test over a sample with a machined hole. Experimental techniques including EBSD, digital image correlation (DIC) and SEM imaging have been used to study crystal orientations, local strain distributions and slip band formation and micro-cracking, respectively. Subsequently, a quasi-2D finite element model (a 3D material model of the microstructure with a thickness of one finite element) of a realistic microstructure, based on EBSD maps, has been generated for simulations adopting an advanced non-local crystal plasticity model (Ma and Hartmaier, 2014), which considers the isotropic hardening and kinematic hardening of plastic strain gradient. In our study, since damage and micro-cracks appear after the first loading cycle, as shown by experimental results reported in Section 2, the accumulated plastic strain is therefore proposed as an important factor for damage and fatigue crack initiation for the investigated material. Based on the simulation results, different FIPs were calculated and compared. Some individual grains and related slip systems were found to be responsible for crack initiation under cyclic loading.

2. Experiment

2.1. Material and methods

The experiment was performed using an aluminium alloy Al2024 T4 received as a 50 mm thick plate. Samples were machined at mid-thickness of the plate. The dimensions of the specimen were 50 mm (length) × 7 mm (width) × 4 mm (thickness), with a 1 mm hole drilled in the center. The corresponding geometry and bending schematic are shown in Fig. 1. The sample was electropolished at the top surface, in a solution containing 30% Nitric acid and 70% Methanol.

EBSD measurements were carried out using a FEI-Sirion SEM, the magnified EBSD map is shown in Fig. 1. After EBSD measurements, the samples were re-polished and then etched to reveal microstructural features such as grain boundaries, particles and inclusions. Cyclic fatigue tests were conducted using a Deben testing stage working inside a CamScan SEM with a cross head speed of 2 mm/min, a frequency of 0.5 Hz and a strain value of approximately 0.01 for the 4-point vertical bending geometries shown in Fig. 1.

The local displacement and strain maps were obtained by means of DIC as described in Efthymiadis (2015) and Alharbi et al. (2015). The features of the microstructure were used to perform the correlation. Measurements were carried out for a flat un-tilted specimen. The microstructure was slightly over-etched to clearly reveal more microstructural features and to increase the contrast of the inclusions and precipitates. The procedure to quantify errors relative to DIC measurements carried out inside a SEM has been reported in Ghadbeigi et al. (2012). Errors for strain values reported in this work are smaller than 0.03 for all images obtained throughout the test. At first the image of the undeformed sample was taken as a reference. Subsequently, consecutive images were obtained at minimum and maximum displacements of each cyclic loading up to 500 cycles. These images were correlated to the reference image to calculate the strain maps.

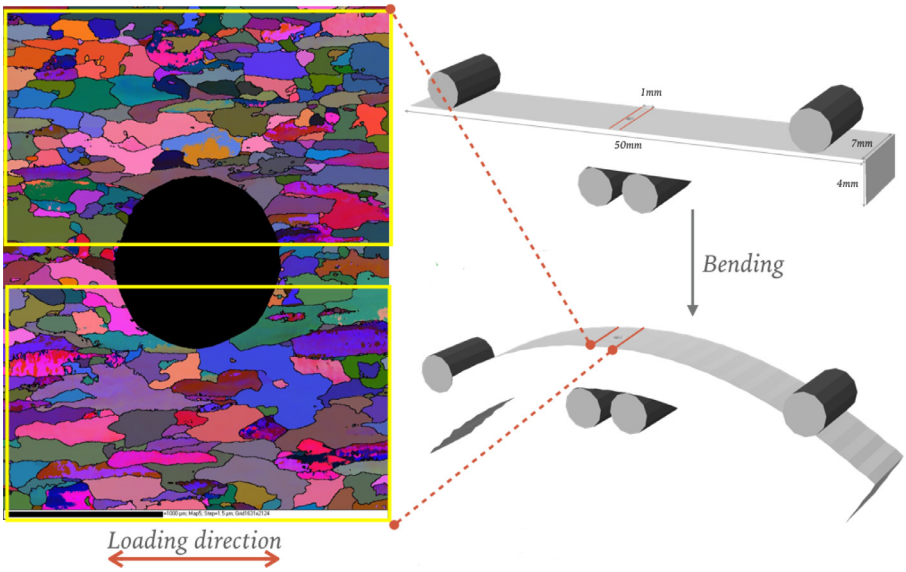

Fig. 1. Schematic drawing of the 4-point bending test with the EBSD map showing the two highlighted regions where DIC analysis was done.

The two yellow boxes on the EBSD map in Fig. 1 show the areas, covering approximately an area of 2.25 mm × 1.5 mm, observed during the in-situ test. The micrographs were analysed using the commercial DIC software, DaVIS 7.0, LAVision to compute the in-plane displacement field from which the strain values were calculated, as explained in (Alharbi et al., 2015). A sensitivity analysis was pursued relative to the interrogation window size. Instead of using a constant interrogation window defined by the number of pixels, a multi-pass procedure of four passes, two passes with 32 × 32 pixels and another two with 16 × 16 pixels was selected for all the experimental results presented in this work. This procedure allows for a progressive reduction of the interrogation window, in order to get accurate measurements of the strains at the grain level. The local strain accuracy is 0.07% with the global strain accuracy 0.0006%. The minimum detectable displacement is 7.8 microns.

Errors due to the SEM imaging system were considered. Errors due to electron beam drift were assessed and were in line with results reported in (Ghadbeigi et al., 2012), with a non-uniform distribution over the analysed area but with magnitudes less than 0.5% which were deemed negligible compared to values up to 75% reported in Fig. 2.

2.2. Experimental results

After the first bending cycle, micro-cracks were found in the two highlighted areas of the strain map (Fig. 2(c) and (d)). The different micro-crack locations infer that grain shape and grain orientation influence the crack initiation process strongly. As shown in Fig. 2(a), the DIC measured major strains are distributed highly non-uniformly over the microstructure. The highest strain magnitudes are observed in regions marked with white triangles near the edge of the central hole. Damage also occurred away from the hole edge within the upper triangle area. This suggests that the strain magnitudes alone are not sufficient to predict crack initiation.

The higher magnification SEM images (Fig. 2(b)–(e)) show different crack formation mechanisms on the sample surface. In one region (Fig. 2(b) and (d)), intense slip bands were observed after the first cycle where a crack initiated after 10 cycles along a slip band. Along the slip bands, micro-voids have nucleated as shown in Fig. 2(c). Irreversible plastic slip and locally excessive plastic deformation are probably the main mechanisms leading to micro-void formation and micro-cracking along the formed slip bands.

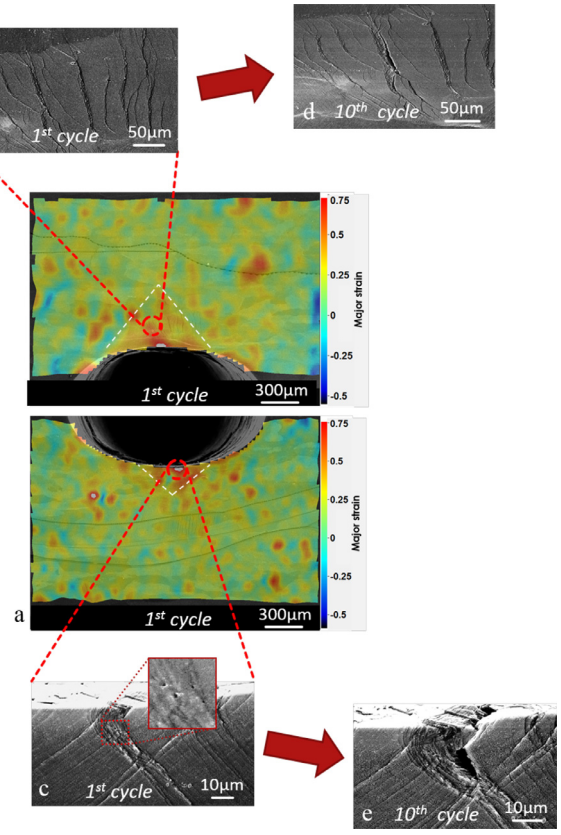

Fig. 2. (a) Local tensile strain measured by DIC, (b)–(e) slip band formation and micro-crack initiation observed in the SEM with microvoids highlighted in (c). The loading direction is horizontal in the images (Efthymiadis, 2015).

3. Simulation

3.1. Microstructure for finite element modelling

In this study, the original EBSD map, shown in Fig. 1, with some modification explained below has been used to generate the cor-

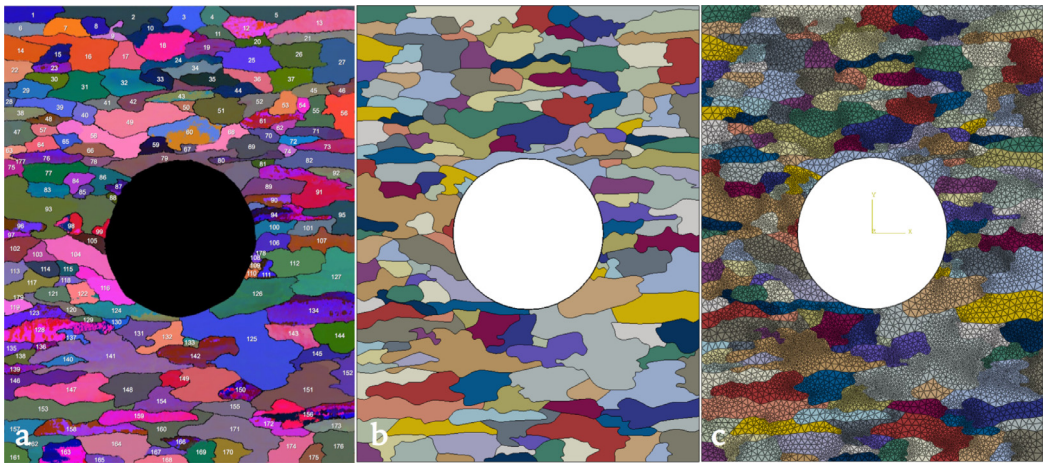

Fig. 3. (a) Original microstructure, (b) simplified microstructure and (c) finite element mesh.

responding microstructure for FEM modelling. Large grains with their orientations and long grain boundaries were kept in the final meshed geometry. Some small grains were deleted. The original and edited images as well as the generated FEM mesh, directly created using Abaqus 6.11, can be seen in Fig. 3. About 90% of the grains with the main features of the experimental microstructure have been captured perfectly. Due to the large grain size, it is expected that the influence of the subsurface grains is minimum. The model has a thickness of one finite element with plane strain conditions. The final microstructure contains 179 grains with different initial orientations. Due to the complex grain geometry, C3D4 (4-node linear tetrahedral) elements had to be used for the simulation. A total of 23,999 elements have been used to reproduce the details of the microstructure.

The displacements at the left and right edges of the DIC map were obtained and imported as boundary conditions into Abaqus. No significant alterations were observed for the displacement vectors at the two (left and right) edges of the DIC map in Fig. 2 during cyclic loading (up to the first 100 cycles).

3.2. The non-local crystal plasticity model

The CPFEM model was developed based on a large total deformation framework. The total deformation gradient $\mathbf{F}$ can be separated into elastic part $\mathbf{F}^{e}$ and plastic part $\mathbf{F}^{p}$ by adopting the multiplicative decomposition approach (Lee, 1969).

$$\mathbf{F} = \mathbf{F}^{e}\mathbf{F}^{p}. \tag{1}$$

Elastic law (Hooke's law) can be defined in the intermediate configuration with the help of the stiffness tensor $\mathbb{C}$ and right Cauchy–Green tensor $C_e = \mathbf{F}^{eT}\mathbf{F}^{e}$ as

$$\widetilde{\mathbf{S}} = \frac{1}{2}\mathbb{C} : \left(\mathbf{F}^{eT}\mathbf{F}^{e} - \mathbf{I}\right), \tag{2}$$

where $\widetilde{\mathbf{S}}$ is the second Piola–Kirchhoff stress defined in the intermediate configuration.

Dislocation slip is the only mechanism considered for plastic deformation, where dislocations glide on well defined slip systems. The widely used constitutive assumption by Asaro and Needleman (1985) and Kalidindi et al. (1992) is adopted in this crystal plasticity model. For the large deformation framework, if the initial plastic deformation gradient $\mathbf{F}^{p0}$ and a small time increment are given, plastic deformation gradient rate can be approximated as

$$\dot{\mathbf{F}}^{p} = \sum_{\alpha=1}^{12} \dot{\gamma}_{\alpha}\widetilde{\mathbf{M}}_{\alpha}\mathbf{F}^{p0}, \tag{3}$$

Table 1
Schmid tensors of the FCC crystal structure.

α	$\widetilde{\mathbf{M}}_{\alpha} = \widetilde{\mathbf{d}}_{\alpha} \otimes \widetilde{\mathbf{n}}_{\alpha}$	α	$\widetilde{\mathbf{M}}_{\alpha} = \widetilde{\mathbf{d}}_{\alpha} \otimes \widetilde{\mathbf{n}}_{\alpha}$
1	$(01\bar{1}) \otimes [111]/\sqrt{6}$	7	$(011) \otimes [1\bar{1}1]/\sqrt{6}$
2	$(10\bar{1}) \otimes [111]/\sqrt{6}$	8	$(10\bar{1}) \otimes [1\bar{1}1]/\sqrt{6}$
3	$(1\bar{1}0) \otimes [111]/\sqrt{6}$	9	$(110) \otimes [1\bar{1}1]/\sqrt{6}$
4	$(\bar{1}11) \otimes [\bar{1}11]/\sqrt{6}$	10	$(011) \otimes [11\bar{1}]/\sqrt{6}$
5	$(101) \otimes [\bar{1}11]/\sqrt{6}$	11	$(101) \otimes [11\bar{1}]/\sqrt{6}$
6	$(110) \otimes [\bar{1}11]/\sqrt{6}$	12	$(1\bar{1}0) \otimes [11\bar{1}]/\sqrt{6}$

where $\dot{\gamma}_{\alpha}$ and $\widetilde{\mathbf{M}}_{\alpha}$ are the shear rate and the Schmid tensor for slip system α, respectively. The list of Schmid tensors of the FCC crystal structure is given in Table 1.

The following flow rule (for each slip system) is used in this study based on Ma and Hartmaier (2014), which incorporates the effect of the non-local hardening terms τ_{α}^{GNDk}, $\hat{\tau}_{\alpha}^{GNDi}$.

$$\dot{\gamma}_{\alpha} = \dot{\gamma}_0 \left| \frac{\tau_{\alpha} + \tau_{\alpha}^{GNDk}}{\hat{\tau}_{\alpha}^{c} + \hat{\tau}_{\alpha}^{GNDi}} \right|^{p_1} \operatorname{sign}(\tau_{\alpha} + \tau_{\alpha}^{GNDk}). \tag{4}$$

In this equation, τ_{α} is the corresponding resolved shear stress of the slip system α, $\hat{\tau}_{\alpha}^{c}$ represents the strain hardening term. $\hat{\tau}_{\alpha}^{GNDi}$ is the isotropic hardening due to first order of plastic strain gradients and τ_{α}^{GNDk} is the kinematic hardening due to second order plastic strain gradients on slip system α. p_1 is the inverse value of the strain rate sensitivity. For small elastic deformation, the resolved shear stress τ can be approximated as

$$\tau_{\alpha} = \widetilde{\mathbf{S}} \cdot \widetilde{\mathbf{M}}_{\alpha}. \tag{5}$$

Typical strain hardening caused by the accumulation of statistically stored dislocations (SSDs) for slip system α can be defined as

$$\dot{\hat{\tau}}_{\alpha}^{c} = \sum_{\beta=1}^{12} h_0 \chi_{\alpha\beta} \left(1 - \frac{\hat{\tau}_{\beta}^{c}}{\hat{\tau}^{sat}}\right)^{p_2} \left|\dot{\gamma}_{\beta}\right|, \tag{6}$$

where $\dot{\gamma}_0$ is the reference shear rate, p_1 is the inverse value of the strain rate sensitivity, h_0 is the initial hardening rate, $\chi_{\alpha\beta}$ is the cross hardening matrix, $\hat{\tau}^{sat}$ is the saturation slip resistance, and p_2 is a fitting parameter.

According to the currently used higher order non-local model (Ma and Hartmaier, 2014), the dislocation density tensor (Nye, 1953; Dai and Parks, 1997) obtained from the first gradient of $\mathbf{F}^{p}$ can be rationalized to 9 super GND components. To evaluate the higher order stresses, gradients of the super GND tensor are approximated as 27 super GND segments. Following the above approach, isotropic and kinematic hardening due to the first and sec-

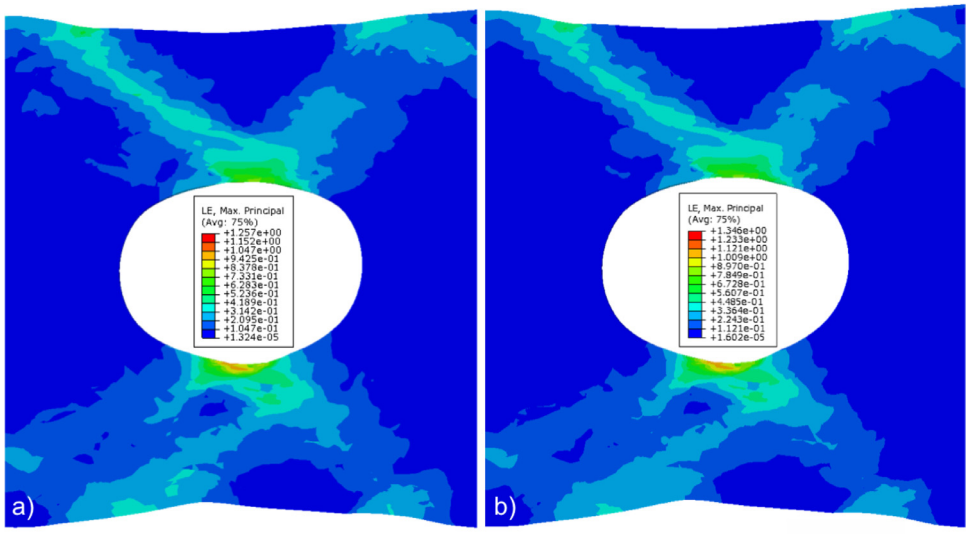

Fig. 4. Maximum principal strain distributions by using a non-local model (a) and a local model (b).

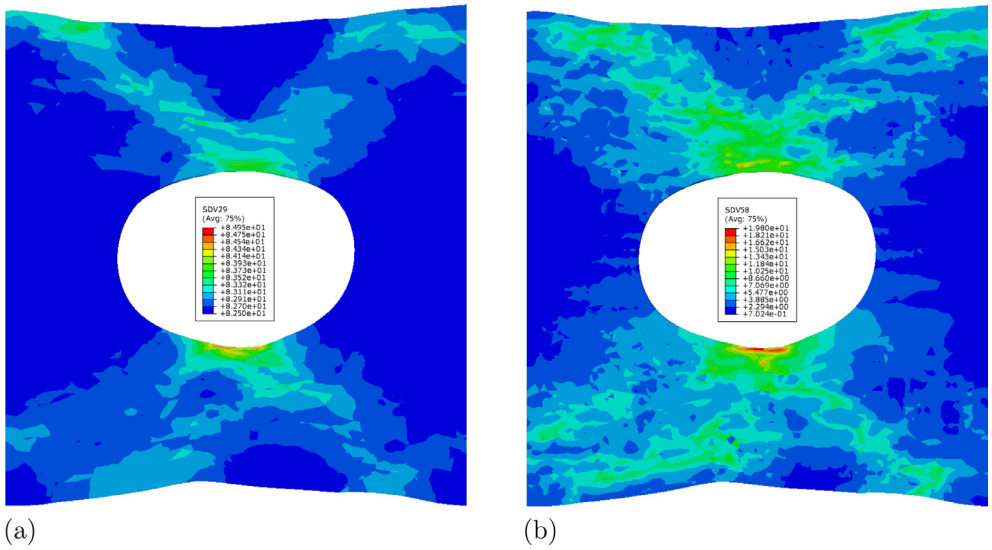

Fig. 5. Hardening distributions in (a) a non-local model with strain hardening (SVD29) and (b) a non-local model with GND hardening (SDV58).

ond order gradients of plastic deformation ($\mathbf{F}^{\mathrm{p}}$) are calculated for slip system α.

$$\hat{\tau}_{\alpha}^{\mathrm{GNDi}} = c^{\mathrm{pass}} \mu b \sqrt{\sum_{\beta=1}^{9} \chi'_{\alpha\beta} \left| A_{\beta ij} \delta_{jkl} \left(\mathbf{F}^{\mathrm{p}} \otimes \nabla \right)_{ikl} \right| / b} \,, \tag{7}$$

$$\tau_{\alpha}^{\mathrm{GNDk}} = \mathbf{F}^{\mathrm{p}} \mathbb{C}' \left(\mathbf{F}^{\mathrm{p}} \otimes \nabla \otimes \nabla \right) \mathbf{F}^{\mathrm{p}\mathrm{T}} \cdot \tilde{\mathbf{M}}_{\alpha}. \tag{8}$$

In Eq. (7), the coefficient c^{pass} is used to calculate the passing stress of crystallographic mobile dislocations due to super GNDs as forest dislocations. Whereas μ, b, $\chi'_{\alpha\beta}$ are model parameters representing shear modulus, Burger vector (magnitude) and interaction matrix between crystallographic mobile dislocations and super GNDs, respectively. Apart from this, δ_{jkl} and $A_{\beta ij}$ in Eq. (7) are the third rank permutation tensor and third order conversion tensor and are used to evaluate the plastic strain gradients. Except for $A_{111} = A_{222} = A_{333} = A_{412} = A_{513} = A_{623} = A_{721} = A_{831} = A_{932} = 1$, the rest of the 72 components of $A_{\beta ij}$ are zero. The sixth order tensor $\mathbb{C}'$ in Eq. (8) depends on the stiffness tensor $\mathbb{C}$ and the average GND pile-up size L. One can refer to the detailed description of non-local terms in Ma and Hartmaier (2014).

Table 2
Non-local crystal plasticity model parameters.

Parameter	Notation	Value
Elastic constant	c_{11}	112 GPa
Elastic constant	c_{12}	59.5 GPa
Elastic constant	c_{44}	24.7 GPa
Shear moduli	μ	48 GPa
Poisson ratio	ν	0.3
Reference shear rate	$\dot{\gamma}_0$	0.001
Inverse of strain rate sensitivity	p_1	20
Initial critical resolved shear stress	$\hat{\tau}_0$	82.5 MPa
Initial hardening rate	h_0	37 MPa
Saturating critical resolved shear stress	$\hat{\tau}_f$	100 MPa
Exponent of strain hardening	p_2	2.25
Cross hardening coefficient	$\chi_{\alpha\beta}$	1.0
Cross hardening coefficient for GND	$\chi_{\alpha\beta}^{\mathrm{GND}}$	1.0
Geometrical factor	c_1	0.1
Average dislocation pile-up size	L	8×10^{-7} m

The list of model parameters is given in Table 2. Values were reported in Luo and Chattopadhyay (2011), Luo (2011) and Efthymiadis (2015). These parameters were calibrated from simple monotonic tensile tests as well as fully reversed cyclic tests.

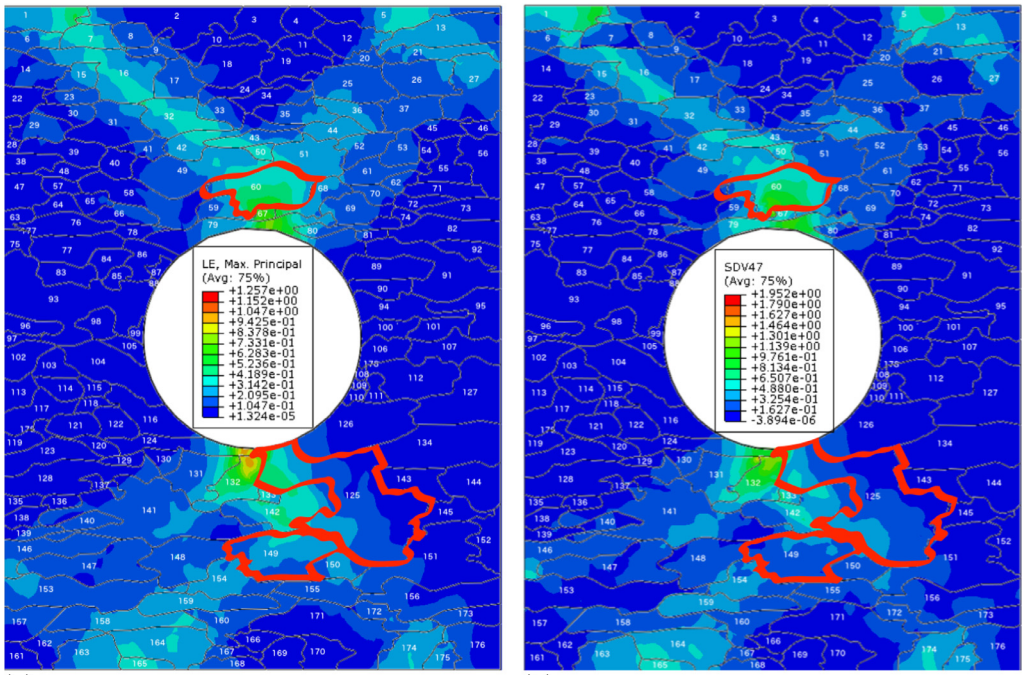

Fig. 6. Distribution of (a) total strain and (b) averaged slip on slip systems (SDV47) in undeformed configuration with grain numbers. Regions having large deformation and grains showing microcrack initiation have been highlighted.

3.3. Simulation results

3.3.1. Strain distributions

The strain gradients which produce isotropic and kinematic hardening strongly depend on grain size and hole size. In order to investigate the non-local hardening, the maximum principal strain distribution for simulations with and without the effect of non-local hardening are compared in Figs. 4 and 5. One can easily see that the non-local hardening of strain gradients only influences some details of the strain distribution; this is due to the fact that the grain size and hole size are rather large. From Fig. 5, GND hardening, only found in the non-local model, is more extensively distributed throughout the microstructure, but with a lower magnitude compared to that of strain hardening in the non-local model. The strain magnitude and heterogeneity in Fig. 5 is higher than that in the experiment. This is likely due to the small area of the microstructure simulated around the hole with the nodes in the upper and lower boundaries treated as free nodes in the simulation. Both the local and non-local model adopted the same model parameters listed in Table 2. The difference in terms of strain distribution is small, but the strain magnitude in the local model is slightly higher than that in the non-local model. This is quite reasonable as the local model is softer than the non-local model. Considering the high resemblance of local and non-local simulation results, in the following part of this paper, only results of the non-local model are reported.

The comparison between total strain and averaged slip on slip systems is given in Fig. 6. The total strain is the von-Mises strain. The accumulated slip is the time integration of the absolute shear rate on slip systems. The averaged slip is the average of accumulated strain of 12 slip systems. The grain boundaries of the grains in which micro-cracks were observed in the experiments are highlighted in Fig. 6. The strain distributions are rather heterogeneous. Although the strain field measured by DIC (Fig. 2(b)) does not show dominating deformation localization bands, a pronounced typical continuous 45° strain localization band at 45° with respect to the tensile direction and a partially continuous 45° plastic strain localization band, in the upper-left part of the sample, is predicted in the simulation. This is due to the simplified boundary conditions adopted in the simulation. The good agreement between strain distributions in the experiment and simulation appears in the regions near to the upper-middle and lower-middle edges of the hole. Most of grain-60 and part of grain-149 are inside these highly strained regions. Since grain-125, for which slip bands and micro-crack initiation were observed experimentally, does not fall in the high strain regions, total strain and averaged slip alone are not sufficient to predict fatigue crack initiation.

3.3.2. Accumulated slip on slip systems

In order to understand and reveal the different mechanisms that drive slip band and micro-crack formation, the accumulated slip on each of the 12 slip systems has been calculated. As shown in Figs. 6 and 7, although the averaged plastic slip inside grain-125 is very low, the accumulated slip on the $(111)[0\bar{1}1]$ slip system is much higher than on other slip systems. Compared to the strong gradients on slip system $(\bar{1}11)[110]$ in grain-60 and on $(11\bar{1})[101]$ in grain-149, plastic slip in grain-125 is much more uniform. For this reason, according to Eq. (8) grain-60 and grain-149 have higher kinematic hardening than grain-125.

Furthermore, with the help of Euler angles in the current configuration, the slip plane normal directions, the slip directions, and the intersection line directions of the slip plane with the sample surface with respect to the dominant slip systems in grain-60, grain-125 and grain-149 have been determined. These lines and directions are superimposed to the experimental image of the microstructure in Fig. 8. The results in the deformed configuration show that the slip planes of slip systems 1, 5 and 10 have different angles with respect to y-direction. These angles, 68.13°, 90.72° and 78.76°, respectively, are in good agreement with the experimental results. Through plotting FEM simulated values at gauss points using the software OVITO, the accumulated slip on four different slip planes was also compared. For example, the combination of slip on the 10^{th}, 11^{th} and 12^{th} slip systems (Fig. 9(d)) supports the

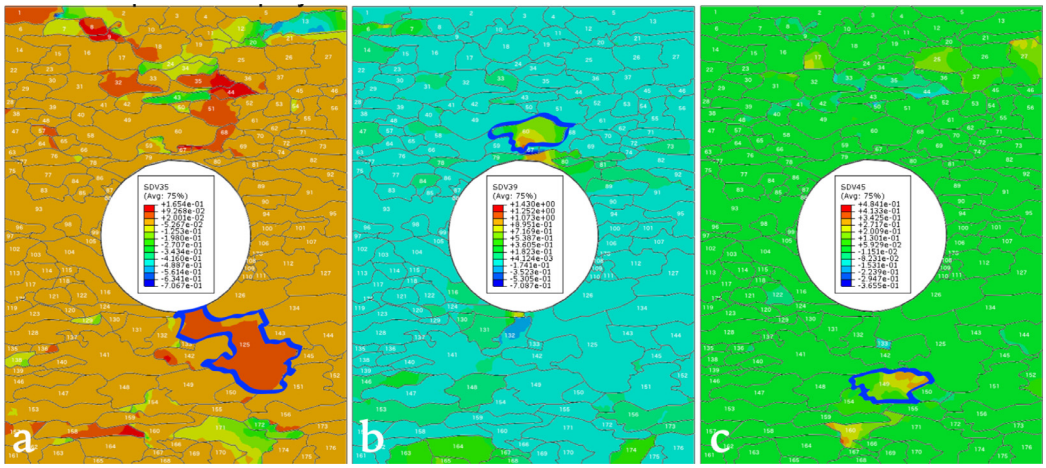

Fig. 7. Accumulated slip on (a) slip system (111)[0$\bar{1}$1] (SDV35), in (b) ($\bar{1}$11)[110] (SDV39) and in (c) (11$\bar{1}$)[101] (SDV45).

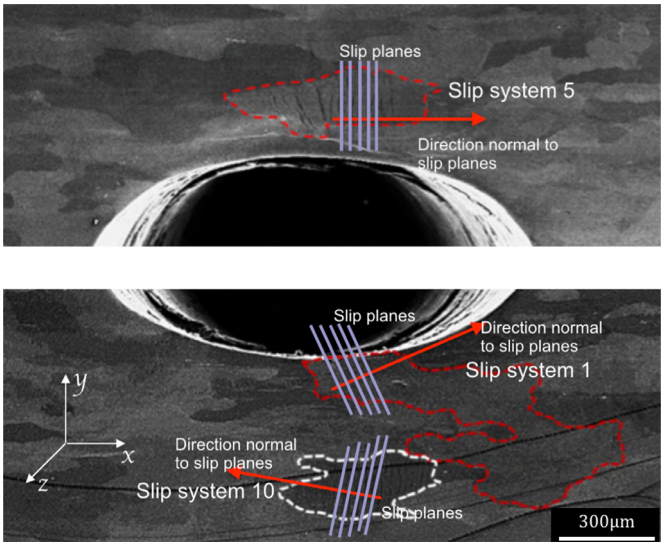

Fig. 8. Comparison between simulated and measured slip band direction.

appearance of slip bands in the three important grains compared to results obtained for the three other cases (Fig. (a)–(c)). These simulations results therefore give some useful insight into the formation of slip bands observed in the SEM images.

3.4. Comparisons of different fatigue indicating parameters

Many fatigue indicating parameters (FIPs) have been proposed in the literature to predict crack initiation (Bozek et al., 2008; Shenoy et al., 2007; Manonukul and Dunne, 2004; Sweeney et al., 2013; Zhang and Jiang, 2006; Przybyla and McDowell, 2010). Very few studies have focused on comparing these parameters. The Fatemi–Socie (FS) parameter was also selected in this study and was calculated inside the Abaqus UMAT subroutine. The FS parameter is defined as:

$$FS = \frac{\Delta\gamma_{\max}}{2}\left(1 + k\frac{\sigma_n^{\max}}{\sigma_y}\right) \tag{9}$$

where $\Delta\gamma_{\max}$ is the maximum range of cyclic plastic shear strain, $\sigma_n^{\max}$ is the peak tensile stress normal to the plane which is associated with maximum shear range, σ_y is the yield strength and k is a constant that is fitted from the uniaxial and torsion fatigue test data.

When $k = 0$, it means that the crack incubation is independent on the normal stress and completely controlled by the irreversible motion of dislocations, in that case FS_{mps} only relates to the maximum range of cyclic plastic shear strain and amounts to:

$$FS_{mps} = \frac{\Delta\gamma_{\max}}{2}. \tag{10}$$

Although the Fatemi–Socie parameter is traditionally used in macroscopic models of fatigue, it has recently been introduced for the prediction of FCI and FCP (fatigue crack propagation) at the microstructural level (Shenoy et al., 2007; Hochhalter et al., 2010, 2011). This parameter therefore depends on the maximal shear strain magnitude variation and the normal stress acting on slip planes. The amount of shear on each slip system was compared at the beginning and at the end of each load cycle to find the magnitude of maximal shear strain variation along with the normal stresses. As the maximal shear is assumed to cause a cleavage type micro-crack parallel to a slip plane, the normal stress on this slip plane is related to the growth of the crack at the microstructural scale.

Fig. 10 shows the *FS* distribution map, with the value of constant k set to 1.2, for both monotonic and cyclic conditions. This parameter does predict correctly crack initiation at the red arrowed locations of Fig. 10. Both locations correspond to the very edge of the hole where crack initiation occurred. There is a slight shift with respect to the location for crack initiation between Fig. 10(a) and (b), moving from monotonic to cyclic loading conditions. The location is better predicted when used cyclic loading conditions in the simulation. However, at the black-arrowed locations, crack initiation is not predicted correctly, as in the simulation (both for monotonic and cyclic) failure occurs at the edge of the hole, while in the experiment it occurs at a distance from the hole. As a result a new FIP parameter is proposed here, which consists of two sub-parameters

$$D^* = \sqrt[(2\alpha+\beta)]{D_1^{2\alpha} \cdot D_3^{\beta}} \tag{11}$$

where D_1 represents the maximum accumulated slip along a specific slip system, and D_3 represents the total accumulated slip over all slip systems (Bozek et al., 2008).

For this study $\alpha = \beta = 1$. The reason for choosing a larger exponent for D_1 is that the maximum slip along a specific slip system leads to the formation of strong slip bands and initiation of fatigue cracks. Furthermore, slip bands also formed outside critically loaded areas but they did not lead to fatigue crack initiation eventually. $(2\alpha + \beta)$ has been used in order to obtain dimensional

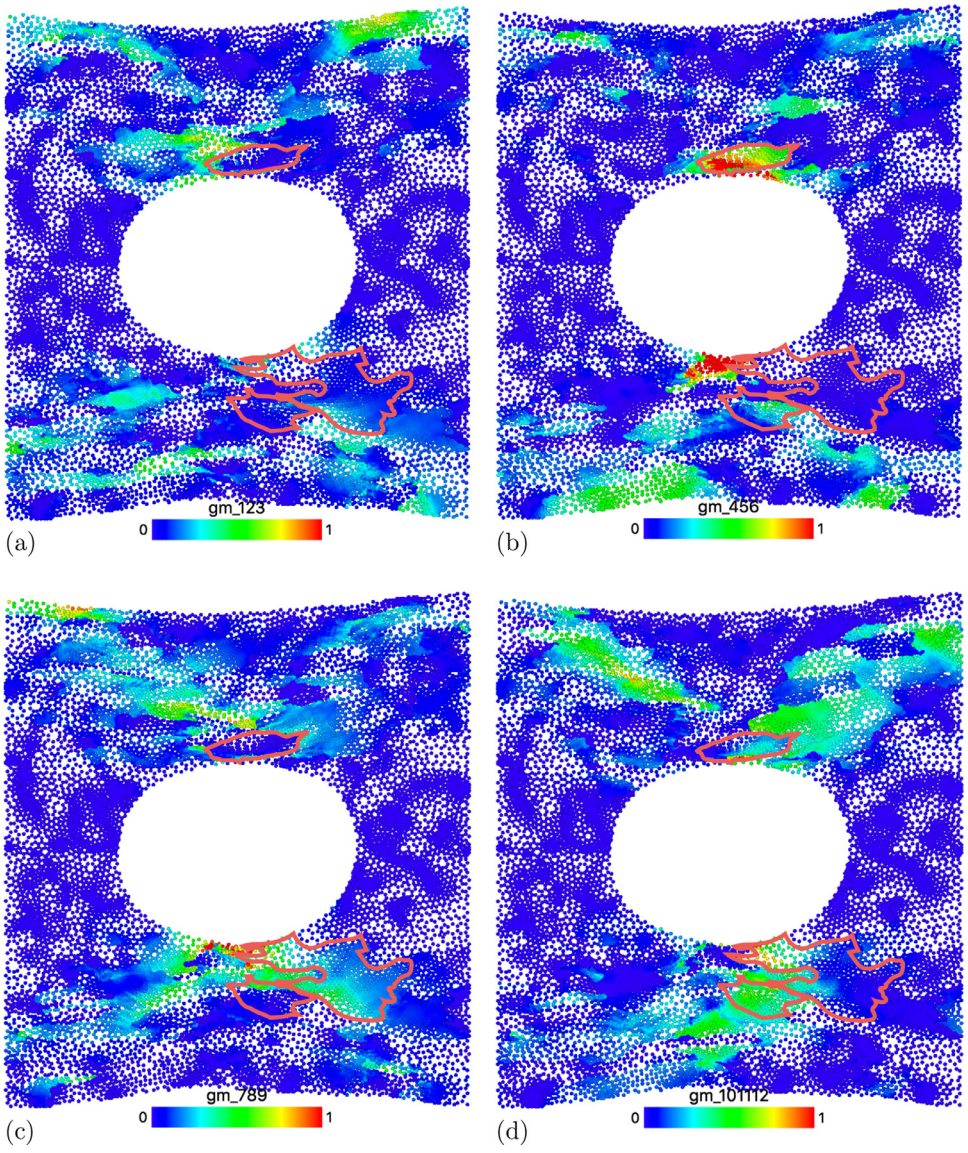

Fig. 9. Distribution of accumulated slips on (a) (111) plane, (b) ($\bar{1}11$) plane, (c) ($1\bar{1}1$) plane, (d) ($11\bar{1}$) plane.

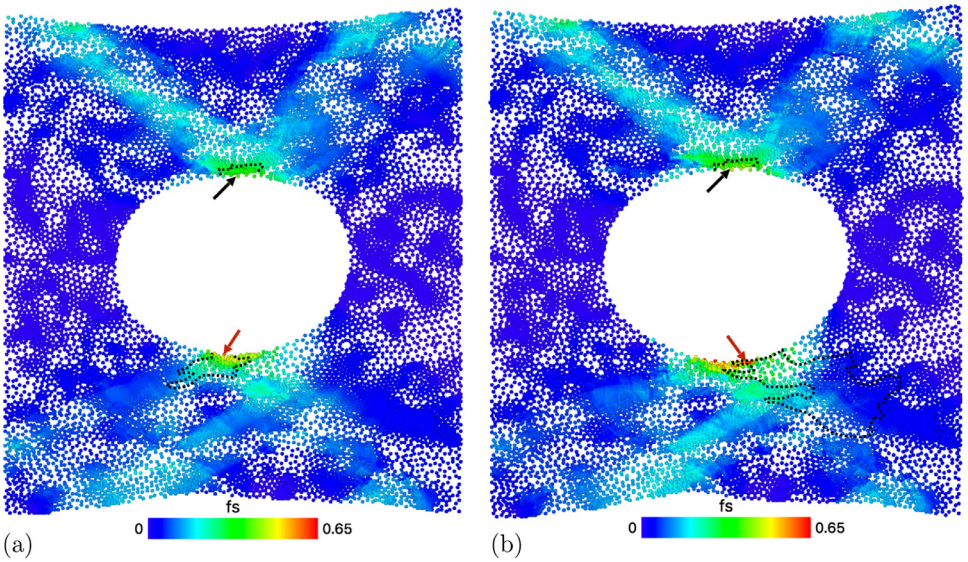

Fig. 10. Comparison of damage predictions by using parameter *FS* in monotonic (a) and cyclic (3 cycles) (b) loading conditions. (For interpretation of the references to colour in this figure, the reader is referred to the web version of this article.)

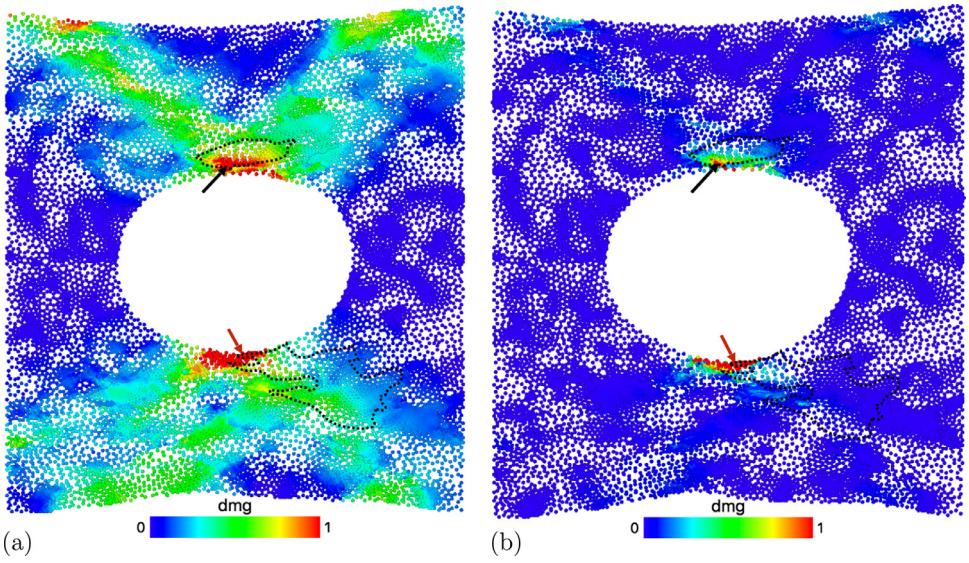

Fig. 11. Comparison of damage predictions by using parameter D^* in monotonic (a) and cyclic (3 cycles) (b) loading conditions. (For interpretation of the references to colour in this figure, the reader is referred to the web version of this article.)

consistency. Fig. 11 shows simulation results when using parameter D^*, with highly damaged areas predicted above and below the central hole. The map shows that crack initiation not only happens along the edge of the hole (red arrows), but also in other locations, close to the edge of the hole as pointed by black arrows. The locations predicted to fail do not change significantly between monotonic and cyclic loading conditions. The effect of grain orientation is more pronounced under cyclic loading conditions in Fig. 11(b). A shear band forms at the red-arrowed location close to the grain boundary of the highlighted grain. This indicates also the advantage of using a non-local CPFE model for predicting behaviours such as shear localisations within grains and strain localisations close to grain boundaries. By comparing Figs. 2, 10 and 11, D^* predicts better the locations where fatigue crack initiation occurs under high amplitude cyclic loading conditions in comparison to the FS parameter. The sub-parameters D_1 and D_3 are both important factors for the prediction of the right locations for fatigue crack nucleation in the microstructure. These results therefore indicate that the Fatemi–Socie parameter is not as effective as the D^* parameter for predicting FCI for the investigated material but is a better predictor for modelling slow crack growth (SCG), as fatigue cracks always initiate along strong slip bands, but tend to deflect towards other directions upon SCG (Shenoy et al., 2007). However further validation of the proposed new criterion through experiments and simulations will be needed in the future.

4. Conclusion

In this paper, slip bands and crack initiation sites at the scale of the microstructure were investigated under cyclic loading using in-situ experiments and CPFEM simulations systematically. Experimental techniques including EBSD, digital image correlation (DIC) and SEM imaging were used to measure grain orientations, local strain distributions, and to analyse slip band and micro-crack formation on the sample surface. A realistic microstructure based on the EBSD map was generated and used for finite element modelling. An advanced non-local crystal plasticity model, which considers the isotropic hardening and kinematic hardening of plastic strain gradient, has been adopted. The simulation results are in good agreement with the experimental results from many aspects:

1. It was found that some individual grains and related slip systems were responsible for crack initiation under cyclic loading.
2. Total plastic strain and averaged plastic slip on all slip systems, combined with accumulated slip on specific slip systems correctly predict the location and orientation of slip bands and micro-cracks.
3. A new fatigue indicating parameter based on the competition between maximum slip along specific slip systems and total plastic slip has been proposed that reproduced the experimental results.

Acknowledgement

The authors are grateful for the financial support provided by EPSRC under the grant EP/F023464/1.

References

Alexandre, F., Deyber, S., Pineau, A., 2004. Modelling the optimum grain size on the low cycle fatigue life of a Ni based superalloy in the presence of two possible crack initiation sites. Scr. Mater. 50 (1), 25–30.
Alharbi, K., Ghadbeigi, H., Efthymiadis, P., Zanganeh, M., Celotto, S., Dashwood, R., Pinna, C., 2015. Damage in dual phase steel dp1000 investigated using digital image correlation and microstructure simulation. Model. Simul. Mater. Sci. Eng. 23 (8), 085005.
Anahid, M., Ghosh, S., 2013. Homogenized constitutive and fatigue nucleation models from crystal plasticity Fe simulations of ti alloys, part 2: Macroscopic probabilistic crack nucleation model. Int. J. Plast. 48, 111–124.
Asaro, R., Needleman, A., 1985. Texture development and strain hardening in rate dependent polycrystals. Acta Metall. 33, 923–953.
Bache, M., Dunne, F., Madrigal, C., 2010. Experimental and crystal plasticity studies of deformation and crack nucleation in a titanium alloy. J. Strain Anal. Eng. Des. 45 (5), 391–399.
Becker, R., Panchanadeeswaran, S., 1995. Effects of grain interactions on deformation and local texture in polycrystals. Acta Metall. Mater. 43 (7), 2701–2719.
Becker, R., Weiland, H., 2000. Use of Ebsd Data in Mesoscale Numerical Analyses. In: Electron Backscatter Diffraction in Materials Science. Springer, pp. 181–198.
Bennett, V., McDowell, D., 2003. Polycrystal orientation distribution effects on microslip in high cycle fatigue. Int. J. Fatigue 25 (1), 27–39.
Bhattacharyya, A., El-Danaf, E., Kalidindi, S.R., Doherty, R.D., 2001. Evolution of grain-scale microstructure during large strain simple compression of polycrystalline aluminum with quasi-columnar grains: oim measurements and numerical simulations. Int. J. Plast. 17 (6), 861–883.
Bobylev, S., Mukherjee, A., Ovidko, I., Sheinerman, A., 2010. Effects of intergrain sliding on crack growth in nanocrystalline materials. Int. J. Plast. 26 (11), 1629–1644.
Bozek, J., Hochhalter, J., Veilleux, M., Liu, M., Heber, G., Sintay, S., Rollett, A., Littlewood, D., Maniatty, A., Weiland, H., et al., 2008. A geometric approach to modeling microstructurally small fatigue crack formation: i. probabilistic simulation of constituent particle cracking in aa 7075-t651. Modell. Simul. Mater. Sci. Eng. 16 (6), 065007.
Brahme, A.P., Inal, K., Mishra, R.K., Saimoto, S., 2011. The backstress effect of evolving deformation boundaries in FCC polycrystals. Int. J. Plast. 27 (8), 1252–1266.

Brückner-Foit, A., Huang, X., 2006. Numerical simulation of micro-crack initiation of martensitic steel under fatigue loading. Int. J. Fatigue 28 (9), 963–971.
Cheong, K.S., Busso, E.P., 2004. Discrete dislocation density modelling of single phase FCC polycrystal aggregates. Acta Mater. 52 (19), 5665–5675.
Cheong, K.S., Smillie, M.J., Knowles, D.M., 2007. Predicting fatigue crack initiation through image-based micromechanical modeling. Acta Mater. 55 (5), 1757–1768.
Choi, S.H., Kim, E.Y., Woo, W., Han, S., Kwak, J., 2013. The effect of crystallographic orientation on the micromechanical deformation and failure behaviors of dp980 steel during uniaxial tension. Int. J. Plast. 45, 85–102.
Christ, H., Dueber, O., Fritzen, C., Knobbe, H., Koester, P., Krupp, U., Kuenkler, B., 2009. Propagation behaviour of microstructural short fatigue cracks in the high-cycle fatigue regime. Comput. Mater. Sci 46, 561–565.
Dai, H., Parks, D., 1997. Geometrically-necessary dislocation density and scale-dependent crystal plasticity. In: Khan, A. (Ed.), Proceedings of Sixth International Symposium on Plasticity, 1. Gordon and Breach, pp. 17–18.
Dunne, F., Wilkinson, A., Allen, R., 2007. Experimental and computational studies of low cycle fatigue crack nucleation in a polycrystal. Int. J. Plast. 23 (2), 273–295.
Efthymiadis, P., 2015. Multiscale experimentation & modeling of fatigue crack development in aluminium alloy 2024. University of Sheffield Ph.D. thesis.
Findley, K.O., 2005. Physically-based models for elevated temperature low cycle fatigue crack initiation and growth in Rene 88DT. Georgia Institute of Technology Ph.D. thesis.
Fine, M.E., Bhat, S.P., 2007. A model of fatigue crack nucleation in single crystal iron and copper. Mater. Sci. Eng. A 468, 64–69.
Ghadbeigi, H., Pinna, C., Celotto, S., 2012. Quantitative strain analysis of the large deformation at the scale of microstructure: comparison between digital image correlation and microgrid techniques. Exp. Mech. 52 (9), 1483–1492.
Hochhalter, J., Littlewood, D., Christ Jr, R., Veilleux, M., Bozek, J., Ingraffea, A., Maniatty, A., 2010. A geometric approach to modeling microstructurally small fatigue crack formation: ii. physically based modeling of microstructure-dependent slip localization and actuation of the crack nucleation mechanism in aa 7075-t651. Modell. Simul. Mater. Sci. Eng. 18 (4), 045004.
Hochhalter, J., Littlewood, D., Veilleux, M., Bozek, J., Maniatty, A., Rollett, A., Ingraffea, A., 2011. A geometric approach to modeling microstructurally small fatigue crack formation: iii. development of a semi-empirical model for nucleation. Modell. Simul. Mater. Sci. Eng. 19 (3), 035008.
Hoshide, T., Kusuura, K., 1998. Life prediction by simulation of crack growth in notched components with different microstructures and under multiaxial fatigue. Fatigue Fract. Eng. Mater. Struct. 21 (2), 201–213.
Huang, X., Brückner-Foit, A., Besel, M., Motoyashiki, Y., 2007. Simplified three-dimensional model for fatigue crack initiation. Eng. Fract. Mech. 74 (18), 2981–2991.
Jablonski, D., 1981. The effect of ceramic inclusions on the low cycle fatigue life of low carbon astroloy subjected to hot isostatic pressing. Mater. Sci. Eng. 48 (2), 189–198.
Kalidindi, S.R., Bronkhorst, C.A., Anand, L., 1992. Crystallographic texture evolution in bulk deformation processing of FCC metals. J. Mech. Phys. Solids 40 (3), 537–569.
Kartal, M., Cuddihy, M., Dunne, F., 2014. Effects of crystallographic orientation and grain morphology on crack tip stress state and plasticity. Int. J. Fatigue 61, 46–58.
Kozaczek, K., Petrovic, B., Ruud, C., Kurtz, S., McIlree, A., 1995. Microstructural modelling of grain-boundary stresses in alloy 600. J. Mater. Sci. 30 (9), 2390–2400.
Kuhlmann-Wilsdorf, D., 1999. The theory of dislocation-based crystal plasticity. Philos. Mag. A 79 (4), 955–1008.
Lee, E., 1969. Elastic-plastic deformation at finite strains. J. Appl. Mech. 36, 1–6.
Li, L., Shen, L., Proust, G., 2015. Fatigue crack initiation life prediction for aluminium alloy 7075 using crystal plasticity finite element simulations. Mech. Mater. 81, 84–93.
Li, Y., Aubin, V., Rey, C., Bompard, P., 2012. Polycrystalline numerical simulation of variable amplitude loading effects on cyclic plasticity and microcrack initiation in austenitic steel 304l. Int. J. Fatigue 42, 71–81.
Luo, C., 2011. Multiscale modeling & virtual sensing for structural health monitoring. Arizona State University Ph.D. thesis.
Luo, C., Chattopadhyay, A., 2011. Prediction of fatigue crack initial stage based on a multiscale damage criterion. Int. J. Fatigue 33 (3), 403–413.
Ma, A., Hartmaier, A., 2014. On the influence of isotropic and kinematic hardening caused by strain gradients on the deformation behaviour of polycrystals. Philos. Mag. 94 (2), 125–140. doi:10.1080/14786435.2013.847290.
Manonukul, A., Dunne, F., 2004. High–and low–cycle fatigue crack initiation using polycrystal plasticity. In: Proc. R. Soc. Lond. A Math. Phys. Eng. Sci., 460, pp. 1881–1903.
Manonukul, A., Dunne, F., Knowles, D., Williams, S., 2005. Multiaxial creep and cyclic plasticity in nickel-base superalloy c263. Int. J. Plast. 21 (1), 1–20.
Mura, T., Nakasone, Y., 1990. A theory of fatigue crack initiation in solids. J. Appl. Mech. 57 (1), 1–6.
Navarro, C., Vázquez, J., Domínguez, J., 2014. 3D vs. 2d fatigue crack initiation and propagation in notched plates. Int. J. Fatigue 58, 40–46.
Nye, J., 1953. Some geometrical relations in dislocated crystals. Acta Metall. 1, 153–162.
Olfe, J., Zimmermann, A., Rie, K., 2000. Simulation of microcrack formation and growth during cyclic loading considering microstructure. INIS Repository 32, 186.
Przybyla, C.P., McDowell, D.L., 2010. Microstructure-sensitive extreme value probabilities for high cycle fatigue of Ni-base superalloy in100. Int. J. Plast. 26 (3), 372–394.
Repetto, E., Ortiz, M., 1997. A micromechanical model of cyclic deformation and fatigue-crack nucleation in FCC single crystals. Acta Mater. 45 (6), 2577–2595.
Robert, C., Saintier, N., Palin-Luc, T., Morel, F., 2012. Micro-mechanical modelling of high cycle fatigue behaviour of metals under multiaxial loads. Mech. Mater. 55, 112–129.
Sangid, M.D., Maier, H.J., Sehitoglu, H., 2011. The role of grain boundaries on fatigue crack initiation–an energy approach. Int. J. Plast. 27 (5), 801–821.
Shenoy, M., Zhang, J., McDowell, D., 2007. Estimating fatigue sensitivity to polycrystalline Ni-base superalloy microstructures using a computational approach. Fatigue Fract. Eng. Mater. Struct. 30 (10), 889–904.
St-Pierre, L., Héripré, E., Dexet, M., Crépin, J., Bertolino, G., Bilger, N., 2008. 3D simulations of microstructure and comparison with experimental microstructure coming from oim analysis. Int. J. Plast. 24 (9), 1516–1532.
Sweeney, C., Vorster, W., Leen, S., Sakurada, E., McHugh, P., Dunne, F., 2013. The role of elastic anisotropy, length scale and crystallographic slip in fatigue crack nucleation. J. Mech. Phys. Solids 61 (5), 1224–1240.
Tanaka, K., Mura, T., 1981. A dislocation model for fatigue crack initiation. J. Appl. Mech. 48 (1), 97–103.
Tsutsumi, S., Toyosada, M., Dunne, F., 2010. Phenomenological cyclic plasticity model for high cycle fatigue. Procedia Eng. 2 (1), 139–146.
Weiland, H., Becker, R., 1999. Analysis of mesoscale deformation structures in aluminum. In: Proceedings of Twentieth Riso International Symposium on Materials Science Deformation-Induced Microstructures: Analysis and Relation to Properties, p. 213.
Xie, C., Fang, Q., Liu, X., Guo, P., Chen, J., Zhang, M., Liu, Y., Rolfe, B., Li, L., 2016. Theoretical study on the deformation twinning and cracking in coarse-grained magnesium alloys. Int. J. Plast. 82, 44–61.
Zhang, H., Diehl, M., Roters, F., Raabe, D., 2016. A virtual laboratory using high resolution crystal plasticity simulations to determine the initial yield surface for sheet metal forming operations. Int. J. Plast. 80, 111–138.
Zhang, J., Jiang, Y., 2006. Fatigue of polycrystalline copper with different grain sizes and texture. Int. J. Plast. 22 (3), 536–556.